

Deblurring 3D Gaussian Splatting

Byeonghyeon Lee^{1*}, Howoong Lee^{2,3*}, Xiangyu Sun², Usman Ali², and Eunbyung Park^{1,2†}

¹ Department of Artificial Intelligence, Sungkyunkwan University

² Department of Electrical and Computer Engineering, Sungkyunkwan University

³ Hanhwa Vision

Abstract. Recent studies in Radiance Fields have paved the robust way for novel view synthesis with their photorealistic rendering quality. Nevertheless, they usually employ neural networks and volumetric rendering, which are costly to train and impede their broad use in various real-time applications due to the lengthy rendering time. Lately 3D Gaussians splatting-based approach has been proposed to model the 3D scene, and it achieves remarkable visual quality while rendering the images in real-time. However, it suffers from severe degradation in the rendering quality if the training images are blurry. Blurriness commonly occurs due to the lens defocusing, object motion, and camera shake, and it inevitably intervenes in clean image acquisition. Several previous studies have attempted to render clean and sharp images from blurry input images using neural fields. The majority of those works, however, are designed only for volumetric rendering-based neural radiance fields and are not straightforwardly applicable to rasterization-based 3D Gaussian splatting methods. Thus, we propose a novel real-time deblurring framework, deblurring 3D Gaussian Splatting, using a small Multi-Layer Perceptron (MLP) that manipulates the covariance of each 3D Gaussian to model the scene blurriness. While deblurring 3D Gaussian Splatting can still enjoy real-time rendering, it can reconstruct fine and sharp details from blurry images. A variety of experiments have been conducted on the benchmark, and the results have revealed the effectiveness of our approach for deblurring. Qualitative results are available at <https://benhenry1.github.io/Deblurring-3D-Gaussian-Splatting/>

1 Introduction

With the emergence of Neural Radiance Fields (NeRF) [23], Novel view synthesis (NVS) has accounted for more roles in computer vision and graphics with its photorealistic scene reconstruction and applicability to diverse domains such as augmented/virtual reality (AR/VR) and robotics. Various NVS methods typically involve modeling 3D scenes from multiple 2D images from arbitrary viewpoints, and these images are often taken under diverse conditions. One of the significant challenges, particularly in practical scenarios, is the common occurrence of blurring effects. It has been a major bottleneck in rendering clean and high-fidelity novel view images, as it requires accurately reconstructing the 3D scene from the blurred input images.

*Equal contribution

†Corresponding authors

NeRF [23] has shown outstanding performance in synthesizing photo-realistic images for novel viewpoints by representing 3D scenes with implicit functions. The volume rendering [7] technique has been a critical component of the massive success of NeRF. This can be attributed to its continuous nature and differentiability, making it well-suited to today’s prevalent automatic differentiation software ecosystems. However, significant rendering and training costs are associated with the volumetric rendering approach due to its reliance on dense sampling along the ray to generate a pixel, which requires substantial computational resources. Despite the recent advancements [10,38,24,8,9] that significantly reduce training time from days to minutes, improving the rendering time still remains a vital challenge.

Recently, 3D Gaussian Splatting (3D-GS) [15] has gained significant attention, demonstrating a capability to produce high-quality images at a remarkably fast rendering speed. It combines a large number of colored 3D Gaussians to represent 3D scenes with a differentiable splatting-based rasterization, substituting NeRF’s time-demanding volumetric rendering. The rendering process projects 3D Gaussian points onto the 2D image planes, and the positions, sizes, rotations, colors, and opacities of these Gaussians are adjusted via gradient-based optimization to better capture the 3D scenes. 3D-GS leverages rasterization, which can be significantly more efficient than volume rendering techniques on modern graphics hardware, thereby enabling rapid real-time rendering.

Expanding on the impressive capabilities of 3D-GS, we aim to further improve its robustness and versatility for more realistic settings, especially those involving blurring effects. Several approaches have attempted to handle the blurring issues in the recent NeRF literature [22,20,6,41,43]. The pioneering work is Deblur-NeRF [22], which renders sharp images from the neural radiance fields and uses an extra multi-layer perceptron (MLP) to produce the blur kernels. DP-NeRF [20] constrains neural radiance fields with two physical priors derived from the actual blurring process to reconstruct clean images. PDRF [28] uses a two-stage deblurring scheme and a voxel representation to further improve deblurring and training time. All works mentioned above have been developed under the assumption of volumetric rendering, which is not straightforwardly applicable to rasterization-based 3D-GS. Another line of works [41,6], though not dependent on volume rendering, only address a specific type of blur, i.e., camera motion blur, and are not valid for mitigating the defocus blur.

In this work, we propose Deblurring 3D-GS, the first defocus deblurring algorithm for 3D-GS, which is well aligned with rasterization and thus enables real-time ren-

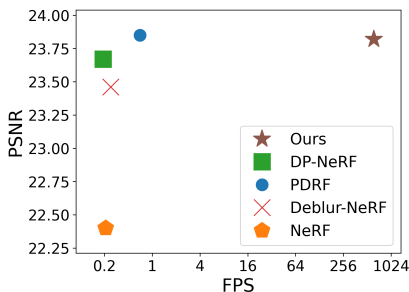


Fig. 1. Performance comparison to state-of-the-art deblurring NeRFs. Ours achieved a fast rendering speed (200 fps vs. 1 fps) while maintaining competitive rendered image quality (x-axis is represented in log scale).

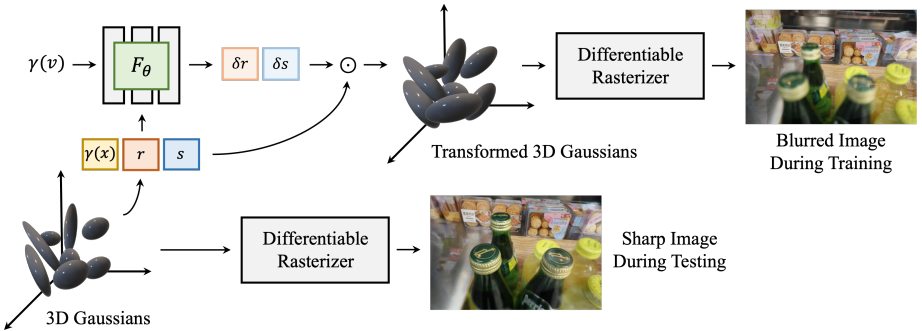


Fig. 2. Our method’s overall workflow. $\gamma(\cdot)$ denotes positional encoding, \odot denotes hadamard product, and x , r , s stand for position, quaternion, and scaling of 3D Gaussian respectively. Given a set of 3D Gaussians G , we extract x , r , s from each 3D Gaussian. Viewing direction v from the dataset and x are positionally encoded and then fed to F_θ , a small MLP parameterized with θ , which yields offsets δr and δs for each Gaussian. These δr and δs are element-wisely multiplied to their respective Gaussians’s r and s respectively, and these computed attributes are used to construct transformed 3D Gaussians $G'(x, r \cdot \delta r, s \cdot \delta s)$. These transformed Gaussians G' are differentially rasterized to render blurred image during training time. However, for inference stage, G is directly fed to differentiable rasterizer, without involving any MLP, to render sharp image.

dering. To do so, we modify the covariance matrices of 3D Gaussians to model the blurriness. Specifically, we employ a small MLP, which manipulates the covariance of each 3D Gaussian to model the scene blurriness. As blurriness is a phenomenon that is based on the intermingling of the neighboring pixels, our Deblurring 3D-GS simulates such an intermixing during the training time. To this end, we designed a framework that utilizes an MLP to learn the variations in different attributes of 3D Gaussians. These small variations are multiplied to the original values of the attributes, which in turn determine the updated shape of the resulting Gaussians. During the inference time, we render the scene using only the original components of 3D-GS without any additional offsets from MLP; thereby, 3D-GS can render sharp images because each pixel is free from the intermingling of nearby pixels. Further, since the MLP is not activated during the inference time, it can still enjoy real-time rendering similar to the 3D-GS while it can reconstruct fine and sharp details from the blurry images.

3D-GS [15] models a 3D scene from a sparse point cloud, which is usually obtained from the structure-from-motion (SfM) [35]. SfM extracts features from multi-view images and relates them via 3D points in the scene. If the given images are blurry, SfM fails heavily in identifying the valid features, and ends up extracting a very small number of points. Even worse, if the scene has a larger depth of field, SfM hardly extracts any points which lie on the far end of the scene. Due to this excessive sparsity in the point cloud constructed from set of blurry images, existing methods, including 3D-GS [15], that rely on point clouds fail to reconstruct the scene with fine details. To compensate for this excessive sparsity, we propose to add extra points with valid color

features to the point cloud using N-nearest-neighbor interpolation [29]. In addition, we prune Gaussians based on their position to keep more Gaussians on the far plane.

A variety of experiments have been conducted on the benchmark, and the results have revealed the effectiveness of our approach for deblurring. Tested under different evaluation matrices, our method achieves state-of-the-art rendering quality or performs on par with the currently leading models while achieving significantly faster rendering speed (> 200 FPS)

To sum up, our contributions are the following:

- We propose the first real-time rendering-enabled defocus deblurring framework using 3D-GS.
- We propose a novel technique that manipulates the covariance matrix of each 3D Gaussian differently to model spatially changing blur using a small MLP.
- To compensate for sparse point clouds due to the blurry images, we propose a training technique that prunes and adds extra points with valid color features so that we can put more points on the far plane of the scene and harshly blurry regions.
- We achieve FPS > 200 while accomplishing superior rendering quality or performing on par with the existing cutting-edge models under different metrics.

2 Related Works

2.1 Image Deblurring

It is common to observe that when we casually take pictures with optical imaging systems, some parts of scene appear blurred in the images. This blurriness is caused by a variety of factors, including object motion, camera shake, and lens defocusing [1,34]. When the image plane is separated from the ideal reference plane during the imaging process, out-of-focus or defocus blur happens. The degradation induced by defocus blur of an image is generally expressed as follows:

$$g(x) = \sum_{s \in S_h} h(x, s) f(x) + n(x), \quad x \in S_f, \quad (1)$$

where $g(x)$ represents an observed blurry image, $h(x, s)$ is a blur kernel or Point Spread Function (PSF), $f(x)$ is a latent sharp image, and $n(x)$ denotes an additive white Gaussian noise that frequently occurs in nature images. $S_f \subset \mathbb{R}^2$ is a support set of an image and $S_h \subset \mathbb{R}^2$ is a support set of a blur kernel or PSF [18].

The first canonical approach to deconvolve an image is [33]. It applies iterative minimization to an energy function to obtain a maximum likelihood approximation of the original image, using a known PSF (the blur kernel). Typically, the blurring kernel K and the sharp image I are unknown. The technique termed as image blind deblurring [42] involves recovering the latent sharp image given just one blurry image B . In this procedure, the deblurred image is obtained by first estimating a blurring kernel. Image blind deblurring is a long-standing and ill-posed problem in the field of image and vision. Numerous approaches to address the blurring issue have been suggested in the literature. Among them, traditional methods often construct deblurring as an optimization problem and rely on natural image priors [21,26,44,47]. Conversely, the majority

of deep learning-based techniques use convolutional neural networks (CNN) to map the blurry image with the latent sharp image directly [25,46,31]. While series of studies have been actively conducted for image deblurring, they are mainly designed for deblurring 2D images and are not easily applicable to 3D scenes deblurring due to the lack of 3D view consistency.

2.2 Neural Radiance Fields

Neural Radiance Fields (NeRF) are a potent method that has recently gained popularity for creating high-fidelity 3D scenes from 2D images. Realistic rendering from novel viewpoints is made possible by NeRF, which uses deep neural networks to encode volumetric scene features. To estimate density $\sigma \in [0, \infty)$ and color value $c \in [0, 1]^3$ of a given point, a radiance field is a continuous function f that maps a 3D location $x \in \mathbb{R}^3$ and a viewing direction $d \in \mathbb{S}^2$. This function has been parameterized by a multi-layer perceptron (MLP) [23], where the weights of MLP are optimized to reconstruct a series of input photos of a particular scene: $(c, \sigma) = f_{\theta} : (\gamma(x), \gamma(d))$. Here, θ indicates the network weights, and γ is the specified positional encoding applied to x and d [39]. To generate the images at novel views, volume rendering [7] is used, taking into account the volume density and color of points.

Fast Inference NeRF Numerous follow-up studies have been carried out to enhance NeRF’s rendering time to achieve real-time rendering. Many methods, such as grid-based approaches [40,4,38,3,8,32], or those relying on hash [24,2] adopt additional data structures to effectively reduce the size and number of layers of MLP and successfully improve the inference speed. However, they still fail to reach real-time view synthesis. Another line of works [30,13,45] proposes to bake the trained parameters into the faster representation and attain real-time rendering. While these methods rely on volumetric rendering, recently, 3D-GS [15] successfully renders photo-realistic images at novel views with noticeable rendering speed using a differentiable rasterizer and 3D Gaussians. Although several approaches have attempted to render tens or hundreds of images in a second, deblurring the blurry scene in real-time is not addressed, while blurriness commonly hinders clean image acquisition in the wild.

Deblurring NeRF Several strategies have been proposed to train NeRF to render clean and sharp images from blurry input images. While DoF-NeRF [43] attempts to deblur the blurry scene, both all-in-focus and blurry images are required to train the model. Deblur-NeRF [22] firstly suggests deblurring NeRF without any all-in-focus images during training. It employs an additional small MLP, which predicts per-pixel blur kernel. However, it has to render the neighboring pixels of the target pixel in advance to model the interference of the neighboring information, so it takes additional computation at the time of training. Though the inference stage does not involve the blur kernel estimation, it is no different from the training with regard to rendering time as it is based on volumetric rendering which takes several seconds to render a single image. DP-NeRF [19] improved Deblur-NeRF in terms of image quality, and PDRF [28] partially replaces MLP to the grid and ameliorates rendering speed, still they depend

on volumetric rendering to produce images and are not free from the rendering cost. Other works [6,41] are aimed at addressing another type of blur, camera motion blur, rather than solving the long rendering time. While these deblurring NeRFs successfully produce clean images from the blurry input images, there is room for improvement in terms of rendering time. Thus, we propose a novel deblurring framework, deblurring 3D Gaussian Splatting, which enables real-time sharp image rendering using a differentiable rasterizer and 3D Gaussians.

3 Deblurring 3D Gaussian Splatting

Based on the 3D-GS [15], we generate 3D Gaussians, and each Gaussian is uniquely characterized by a set of the parameters, including 3D position x , opacity σ , and covariance matrix derived from quaternion r scaling s . Each 3D Gaussian also contains spherical harmonics (SH) to represent view-dependent appearance. The input for the proposed method consists of camera poses and point clouds, which can be obtained through the structure from motion (SfM) [35], and a collection of images (possibly blurred). To deblur 3D Gaussians, we employ an MLP that takes the positions of the 3D Gaussians along with the r and s as inputs and outputs δr , and δs which are the small scaling factors multiplied to r and s , respectively. With new quaternion and scale, $r \cdot \delta r$ and $s \cdot \delta s$, the updated 3D Gaussians are subsequently fed to the tile-based rasterizer to produce the blurry images. The overview of our method is shown in Fig. 2.

3.1 Differential Rendering via 3D Gaussian Splatting

At the training time, the blurry images are rendered in a differentiable way and we use a gradient-based optimization to train our deblurring 3D Gaussians. We adopt methods from [15], which proposes differentiable rasterization. Each 3D Gaussian is defined by its covariance matrix $\Sigma(r, s)$ with mean value in 3D world space x as following:

$$G(x, r, s) = e^{-\frac{1}{2}x^T \Sigma^{-1}(r, s)x}. \quad (2)$$

Besides $\Sigma(r, s)$ and x , 3D Gaussians are also defined with spherical harmonics coefficients (SH) to represent view-dependent appearance and opacity for alpha value. The covariance matrix is valid only when it satisfies positive semi-definite, which is challenging to constrain during the optimization. Thus, the covariance matrix is decomposed into two learnable components, a quaternion r for representing rotation and s for representing scaling, to circumvent the positive semi-definite constraint similar to the configuration of an ellipsoid. r and s are transformed into rotation matrix and scaling matrix, respectively, and construct $\Sigma(r, s)$ as follows:

$$\Sigma(r, s) = R(r)S(s)S(s)^T R(r)^T, \quad (3)$$

where $R(r)$ is a rotation matrix given the rotation parameter r and $S(s)$ is a scaling matrix from the scaling parameter s [17]. These 3D Gaussians are projected to 2D space [48] to render 2D images with following 2D covariance matrix $\Sigma'(r, s)$:

$$\Sigma'(r, s) = JW \Sigma(r, s)W^T J^T, \quad (4)$$

where J denotes the Jacobian of the affine approximation of the projective transformation, W stands for the world-to-camera matrix. Each pixel value is computed by accumulating N ordered projected 2D Gaussians overlaid on the each pixel with the formula:

$$C = \sum_{i \in N} T_i c_i \alpha_i \quad \text{with} \quad T_i = \prod_{j=1}^{i-1} (1 - \alpha_j), \quad (5)$$

c_i is the color of each point, and T_i is the transmittance. $\alpha_i \in [0, 1]$ defined by $1 - \exp^{-\sigma_i \delta_i}$ where σ_i and δ_i are the density of the point and the interval along the ray respectively. For further details, please refer to the original paper [15].

3.2 Deblurring 3D Gaussians

Motivation It is discussed in section 2.1 that the pixels in images get blurred due to defocusing, and this phenomenon is usually modeled through a convolution operation. According to the thin lens law [12], the scene points that lie at the focal distance of the camera make a sharp image at the imaging plane. On the other hand, any scene points that are not at the focal distance will make a blob instead of a sharp point on the imaging plane, and it produces a blurred image. If the separation from the focal distance of a scene point is large, it produces a blob of a large area, which corresponds to severe blur. This blurring effect is usually modeled by a 2D Gaussian function known as the point spread function (PSF). Correspondingly, an image captured by a camera is the result of the convolution of the actual image and the PSF. Through this convolution, which is the weighted summation of neighboring pixels, few pixels can affect the central pixel heavily depending on the weight. In other words, in the defocus imaging process, a pixel affects the intensity of neighboring pixels. This theoretical base provides us the motivation to build our deblurring 3D Gaussians framework. We assume that big sized 3D Gaussians cause the blur, while relatively smaller 3D Gaussians correspond to the sharp image. This is because those with greater dispersion are affected by more neighboring information as they are responsible for wider regions in image space, so they can represent the interference of the neighboring pixels. Whereas the fine details in the 3D scene can be better modeled through the smaller 3D Gaussians.

Modelling Following the above mentioned motivation, we learn to deblur by transforming the geometry of the 3D Gaussians. The geometry of the 3D Gaussians is expressed through the covariance matrix, which can be decomposed into the rotation and scaling factors as mentioned in Eq. 3. Therefore, our target is to change the rotation and scaling factors of 3D Gaussians in such a way that we can model the blurring phenomenon. To do so, we have employed an MLP that takes the position x , rotation r , scale s , and viewing direction v of 3D Gaussians as inputs, and outputs $(\delta r, \delta s)$, as given by:

$$(\delta r, \delta s) = \mathcal{F}_\theta \left(\gamma(x), r, s, \gamma(v) \right), \quad (6)$$

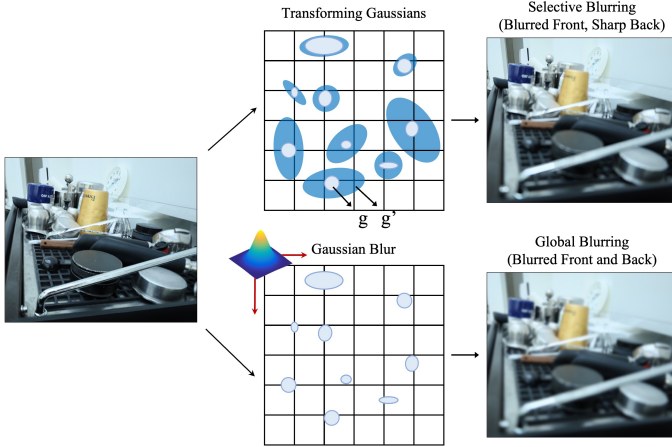


Fig. 3. Comparison to normal Gaussian blur kernel. Top row: It shows the proposed method. g is the Gaussian before the transformation, and g' is the Gaussian after the transformation. Since the different transformations can be applied to different Gaussian, ours can selectively blur the images depending on the scene; it can only blur the front parts of the scene. Bottom row: It shows a normal Gaussian blur kernel, which is not capable of handling different parts of the image differently, thereby uniformly blurring the entire image.

where \mathcal{F}_θ denotes the MLP, and γ denotes the positional encoding which is defined as:

$$\gamma(p) = (\sin(2^k \pi p), \cos(2^k \pi p))_{k=0}^{L-1}, \quad (7)$$

where L is the number of the frequencies, and the positional encoding is applied to each element of the vector p [23].

The minima of these scaling factors ($\delta r, \delta s$) are clipped to 1 and element-wisely multiplied to r and s , respectively, to obtain the transformed attributes $r' = r \cdot \delta r$ and $s' = s \cdot \delta s$. With these transformed attributes, we can construct the transformed 3D Gaussians $G(x, r', s')$, which is optimized during training to model the scene blurriness. As s' is greater than or equal to s , each 3D Gaussian of $G(x, r', s')$ has greater statistical dispersion than the original 3D Gaussian $G(x, r, s)$. With the expanded dispersion of 3D Gaussian, it can represent the interference of the neighboring information which is a root cause of defocus blur. In addition, $G(x, r', s')$ can model the blurry scene more flexibly as per-Gaussian δr and δs are estimated. Defocus blur is spatially-varying, which implies different regions has different levels of blurriness. The scaling factors for 3D Gaussians that are responsible for a region with harsh defocus blur where various neighboring information in wide range is involved in, becomes bigger to better model high degree of blurriness. Those for 3D Gaussians on the sharp area, on the other hand, are closer to 1 so that they have smaller dispersion and do not represent the influence of the nearby information.

At the time of inference, we use $G(x, r, s)$ to render the sharp images. As mentioned earlier, we assume that multiplying two different scaling factors to transform the geom-

etry of 3D Gaussians can work as blur kernel and convolution in section 2.1. Thus, $G(x, r, s)$ can produce the images with clean and fine details. It is worth noting that since any additional scaling factors are not used to render the images at testing time, F_θ is not activated so all steps required for the inference of Deblurring 3D-GS are identical to 3D-GS, which in turn enables real-time sharp image rendering. In terms of training, only forwarding F_θ and simple element-wise multiplication are extra cost.

Selective blurring The proposed method can handle the training images arbitrarily blurred in various parts of the scene. Since we predict $(\delta r, \delta s)$ for each Gaussian, we can selectively enlarge the covariances of Gaussians where the parts in the training images are blurred. Such transformed per-Gaussian covariance is projected to 2D space and it can act as pixel-wise blur kernel at the image space. It is noteworthy that applying different shapes of blur kernels to different pixels plays a pivotal role in modeling scene blurriness since blurriness spatially varies. This flexibility enables us to effectively implement deblurring capability in 3D-GS. On the other hand, a naive approach to blurring the rendered image is simply to apply a Gaussian kernel. As shown in Fig. 3, this approach will blur the entire image, not blur pixel-wisely, resulting in blurring parts that should not be blurred for training the model. Even if learnable Gaussian kernel is applied, optimizing the mean and variance of the Gaussian kernel, a single type of blur kernel is limited in its expressivity to model the complicatedly blurred scene and is optimized to model the average blurriness of the scene from averaging loss function which fails to model blurriness morphing in each pixel. Not surprisingly, the Gaussian blur is a special case of the proposed method. If we predict one (δs) for all 3D Gaussians, then it will similarly blur the whole image.

Algorithm 1 Add Extra Points

Require: \mathcal{P} : Point cloud computed from SfM

Require: K : Number of the neighboring points to find

Require: N_p : Number of additional points to generate

Require: t_d : Minimum required distance between new point and existing point

$P_{\text{add}} \leftarrow \text{GenerateRandomPoints}(\mathcal{P}, N_p)$ ▷ Uniformly sample N_p points

for each p in P_{add} **do**

$\mathcal{P}_{\text{knn}} \leftarrow \text{FindNearestNeighbors}(\mathcal{P}, p, K)$ ▷ Get K nearest points of p from \mathcal{P}

$\mathcal{P}_{\text{valid}} \leftarrow \text{CheckDistance}(\mathcal{P}_{\text{knn}}, p, t_d)$ ▷ Discard irrelevant neighbors

if $|\mathcal{P}_{\text{valid}}| > 0$ **then**

$p_c \leftarrow \text{LinearInterpolate}(\mathcal{P}_{\text{valid}}, p)$ ▷ Linearly interpolate neighboring colors

$\text{AddToPointCloud}(\mathcal{P}, p, p_c)$

end if

end for

3.3 Compensation for Sparse Point Cloud

3D-GS [15] constructs multiple 3D Gaussians from point clouds to model 3D scenes, and its reconstruction quality heavily relies on the initial point clouds. Point clouds are

generally obtained from the structure-from-motion (SfM) [36], which extracts features from multi-view images and relates them to several 3D points. However, it can produce only sparse point clouds if the given images are blurry due to the challenge of feature extraction from blurry inputs. Even worse, if the scene has a large depth of field, which is prevalent in defocus blurry scenes, SfM hardly extracts any points that lie on the far end of the scene. To make a dense point cloud, we add additional points after N_{st} iterations. N_p points are sampled from an uniform distribution $U(\alpha, \beta)$ where α and β are the minimum and maximum value of the position of the points from the existing point cloud, respectively. The color for each new point p is assigned with the interpolated color p_c from the nearest neighbors \mathcal{P}_{knn} among the existing points using K-Nearest-Neighbor (KNN) [29]. We discard the points whose distance to the nearest neighbor exceeds the distance threshold t_d to prevent unnecessary points from being allocated to the empty space. The process of adding extra points to the given point cloud is summarized in algorithm 1. fig. 5 shows that a point cloud with additional points has a dense distribution of points to represent the objects.

Furthermore, 3D-GS [15] effectively manages the number of 3D Gaussians (the number of points) through periodic adaptive density control, densifying and pruning 3D Gaussians. To compensate for the sparsity of 3D Gaussians lying on the far end of the scene, we prune 3D Gaussians depending on their positions. As the benchmark Deblur-NeRF dataset [22] consists of only forward-facing scenes, the z-axis value of each point can be a relative depth from any viewpoints. As shown in fig. 4, we prune out less 3D Gaussians placed on the far edge of the scene to preserve more points located at the far plane, relying on the relative depth. Specifically, the pruning threshold t_p is scaled by w_p to 1.0 depending on the relative depth, and the lowest threshold is applied to the farthest point. Densifying more for far-plane-3D Gaussians is also an available option, but excessive compensation hinders modeling the scene blurriness, and it can further degrade real-time rendering as extra computational cost is required. We empirically found that flexible pruning was enough to compensate for sparse point cloud, considering the rendering speed. fig. 6 shows that relative depth-based pruning preserves the points lying on the far plane of the scene and leads to successful reconstruction of the objects on the far plane.

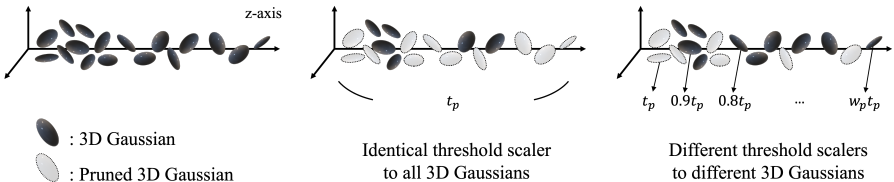


Fig. 4. Comparison to pruning 3D Gaussians. Left: Given 3D Gaussians. Middle: Applying pruning method proposed by 3D-GS which removes 3D Gaussians with the single threshold (t_p). Right: Our pruning method which discards unnecessary 3D Gaussians with different thresholds based upon their depth.

Table 1. Quantitative results on real defocus dataset. We color each cell as **best** and **second best**. *3D-GS achieved the highest FPS because it failed to model the blurry scene, abnormally small number of 3D Gaussians are in use which in turn raises FPS.

	Cake		Caps		Cisco		Coral		Cupcake		Average	FPS	
	PSNR↑	SSIM↑	PSNR↑	SSIM↑	PSNR↑	SSIM↑	PSNR↑	SSIM↑	PSNR↑	SSIM↑			PSNR↑
NeRF [23]	24.42	0.7210	22.73	0.6312	20.72	0.7217	19.81	0.5658	21.88	0.6809			
3D-GS [15]	20.16	0.5903	19.08	0.4355	20.01	0.6931	19.50	0.5519	21.53	0.6794			
Deblur-NeRF [22]	26.27	0.7800	23.87	0.7128	20.83	0.7270	19.85	0.5999	22.26	0.7219			
DP-NeRF [19]	26.16	0.7781	23.95	0.7122	20.73	0.7260	20.11	0.6107	22.80	0.7409			
PDRF-10 [28]	27.06	0.8032	24.06	0.7102	20.68	0.7239	19.61	0.5894	22.95	0.7421			
Ours	27.08	0.8076	24.68	0.7437	21.06	0.7409	20.24	0.5617	22.65	0.7477			
	Cups		Daisy		Sausage		Seal		Tools		Average	FPS	
	PSNR↑	SSIM↑	PSNR↑	SSIM↑	PSNR↑	SSIM↑	PSNR↑	SSIM↑	PSNR↑	SSIM↑			PSNR↑
NeRF [23]	25.02	0.7581	22.74	0.6203	17.79	0.4830	22.79	0.6267	26.08	0.8523	22.40	0.6661	< 1
3D-GS [15]	20.55	0.6459	20.96	0.6004	17.83	0.4718	22.25	0.5905	23.82	0.805	20.57	0.6064	788*
Deblur-NeRF [22]	26.21	0.7987	23.52	0.6870	18.01	0.4998	26.04	0.7773	27.81	0.8949	23.46	0.7199	< 1
DP-NeRF [19]	26.75	0.8136	23.79	0.6971	18.35	0.5443	25.95	0.7779	28.07	0.8980	23.67	0.7299	< 1
PDRF-10 [28]	26.39	0.8066	24.49	0.7426	18.94	0.5686	26.36	0.7959	28.00	0.8995	23.85	0.7382	< 1
Ours	26.26	0.8240	23.70	0.7268	18.74	0.5539	26.25	0.8197	27.58	0.9037	23.82	0.7430	620

Table 2. Quantitative results on synthetic defocus dataset. We color each cell as **best** and **second best**. *3D-GS achieved the highest FPS because it failed to model the blurry scene, abnormally small number of 3D Gaussians are in use which in turn raises FPS.

	Cozyroom		Factory		Pool		Tanabata		Trolley		Average	FPS	
	PSNR↑	SSIM↑	PSNR↑	SSIM↑	PSNR↑	SSIM↑	PSNR↑	SSIM↑	PSNR↑	SSIM↑			PSNR↑
NeRF [23]	30.03	0.8926	25.36	0.7847	27.77	0.7266	23.90	0.7811	22.67	0.7103	25.93	0.7791	< 1
3D-GS [15]	30.09	0.9024	24.52	0.8057	20.14	0.4451	23.08	0.7981	22.26	0.7400	24.02	0.7383	789*
Deblur-NeRF [22]	31.85	0.9175	28.03	0.8628	30.52	0.8246	26.26	0.8517	25.18	0.8067	28.37	0.8527	< 1
DP-NeRF [19]	32.11	0.9215	29.26	0.8793	31.44	0.8529	27.05	0.8635	26.79	0.8395	29.33	0.8713	< 1
PDRF-10 [28]	32.29	0.9305	30.90	0.9138	30.97	0.8408	28.18	0.9006	28.07	0.8799	30.08	0.8931	< 1
Ours	32.03	0.9269	29.89	0.9096	30.50	0.8344	27.56	0.9071	27.18	0.8755	29.43	0.8907	663

4 Experiments

We compared our method against the state-of-the-art deblurring approaches in neural rendering: Deblur-NeRF [22], DP-NeRF [20], PDRF [28] and original 3D Gaussians Splatting (3D-GS) [15]

4.1 Experimental Settings

We utilized PyTorch [27] to create our deblurring pipeline while maintaining the differentiable Gaussian rasterization 3D-GS [15]. We conducted 30k iterations of training. Adam optimizer [16] is used for optimization with the identical setting of 3D-GS. We set the learning rate for MLP at 1e-3, and the rest parameters are identical to 3D-GS. We use MLP with 3 hidden layers, each layer having 64 hidden units and ReLU activation. MLP is initialized with Xavier initialization [11]. For adding extra points to compensate the sparse point cloud, we set the addition start iteration N_{st} to 2,500, the number of supplementing points N_p to 100,000, the number of neighbors K to 4, and

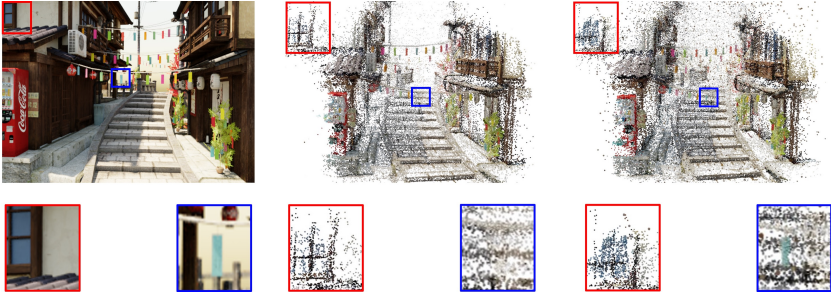


Fig. 5. Comparison on densifying point clouds during training. Left: Example training view. Middle: Point cloud at 5,000 training iterations without adding points. Bottom: Point cloud at 5,000 training iterations with adding extra points at 2,500 iterations.

the minimum distance threshold t_d to 10. In terms of depth-based pruning, t_p for pruning threshold is set to $5e-3$ and 0.3 is used for w_p , the pruning threshold scaler. All the experiments were conducted on NVIDIA RTX 4090 GPU with 24GB memory.

We evaluated the performance on the benchmark Deblur-NeRF dataset [22] that includes both synthetic and real defocus blurred images. This dataset contains five scenarios in the synthetic defocus category and ten in the real defocus category. Synthetic defocus images are constructed using Blender [5]. By setting the aperture size and randomly selecting a focal plane between the closest and farthest depths, realistic defocus blur effects were produced. COLMAP [36,37] is used to calculate the camera position of the blur and reference image in the real scene after choosing a big aperture to capture the defocus image.

4.2 Results and Comparisons

In this section, we provide the outcomes of our experiments, presenting a thorough analysis of both qualitative and quantitative results. Our evaluation framework encompasses a diverse set of metrics to show a comprehensive assessment of the experimental results. Primarily, we rely on established metrics such as the Peak Signal-to-Noise Ratio (PSNR), Structural Similarity Index (SSIM), and Frames Per Second (FPS).

First of all, we show the transformation in the values of two Gaussian attributes (scale and rotation) to model the blur. The average values of these two attributes have been mentioned in Table 3. These values have been computed for all the scenes in real defocus dataset. It can be seen that during training, as compared to testing, 3D Gaussians of larger values of scale and rotation have been used to rasterize the scene. This indicates that larger values of scale and rotation are needed to adjust the 3D Gaussians to rasterize the blurred (training) images. While, in contrast, smaller values of these two attributes demonstrate that the smaller sized Gaussians are more suitable to model the fine details that are present in the sharp (testing) images.

As shown in table 1 and fig. 1 our method is on par with the state-of-the-art model in PSNR and achieve state-of-the-art performance evaluated under SSIM on the real defocus dataset. At the same time, it can still enjoy real-time rendering, with noticeable



Fig. 6. Comparison on applying depth-based pruning. Top: Rendered image from the model with depth-dependent pruning. Bottom: Rendered image from the model with naive pruning as 3D-GS does.

FPS, compared to other deblurring models. Also, table 2 shows the quantitative result on the synthetic defocus dataset. FPS of 3D-GS is abnormally high because it fails to model the blurry scene, thus only small number of 3D Gaussians are created. fig. 7 and fig. 8 show the qualitative results on real and synthetic defocus dataset, respectively. We can see that ours can produce sharp and fine details, while 3D-GS fail to reconstruct those details.

4.3 Ablation Study

Extra points allocation In this section, we evaluate the effect of adding extra points to the sparse point cloud. As shown in fig. 5, directly using sparse point cloud without any point densification only represents the objects with a small number of points or totally fails to model the tiny objects. Meanwhile, in case extra points are added to the point cloud, points successfully represent the objects densely. Also, the quantitative result is presented in table 4. It shows assigning valid color features to the additional points is important to deblur the scene and reconstruct the fine details.

Depth-based pruning We conduct an ablation study on depth-based pruning. To address excessive sparsity of point cloud at the far plane, we prune the points on the far plane less to maintain more numbers of points. table 5 shows there is severe rendering quality degradation if naive pruning, prunes the points with the same threshold from near plane to far plane, is used. In addition, fig. 6 shows a failure to reconstruct objects at the far plane when naive pruning is used, while objects lying on the near-end of the scene are well reconstructed. Meanwhile, ours, with depth-based pruning, can render clean objects on both near and far planes.

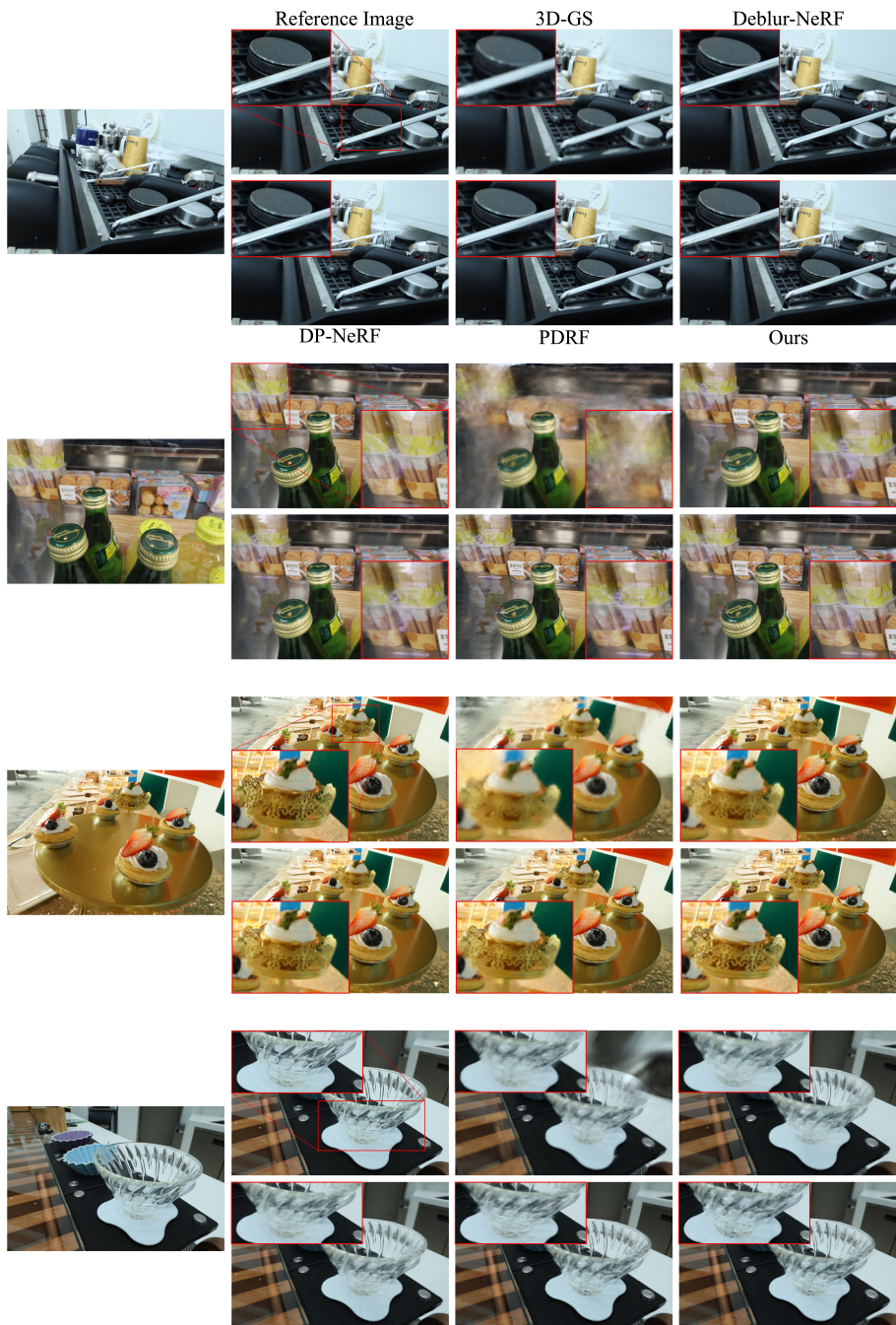


Fig. 7. Qualitative results on real defocus blur dataset.

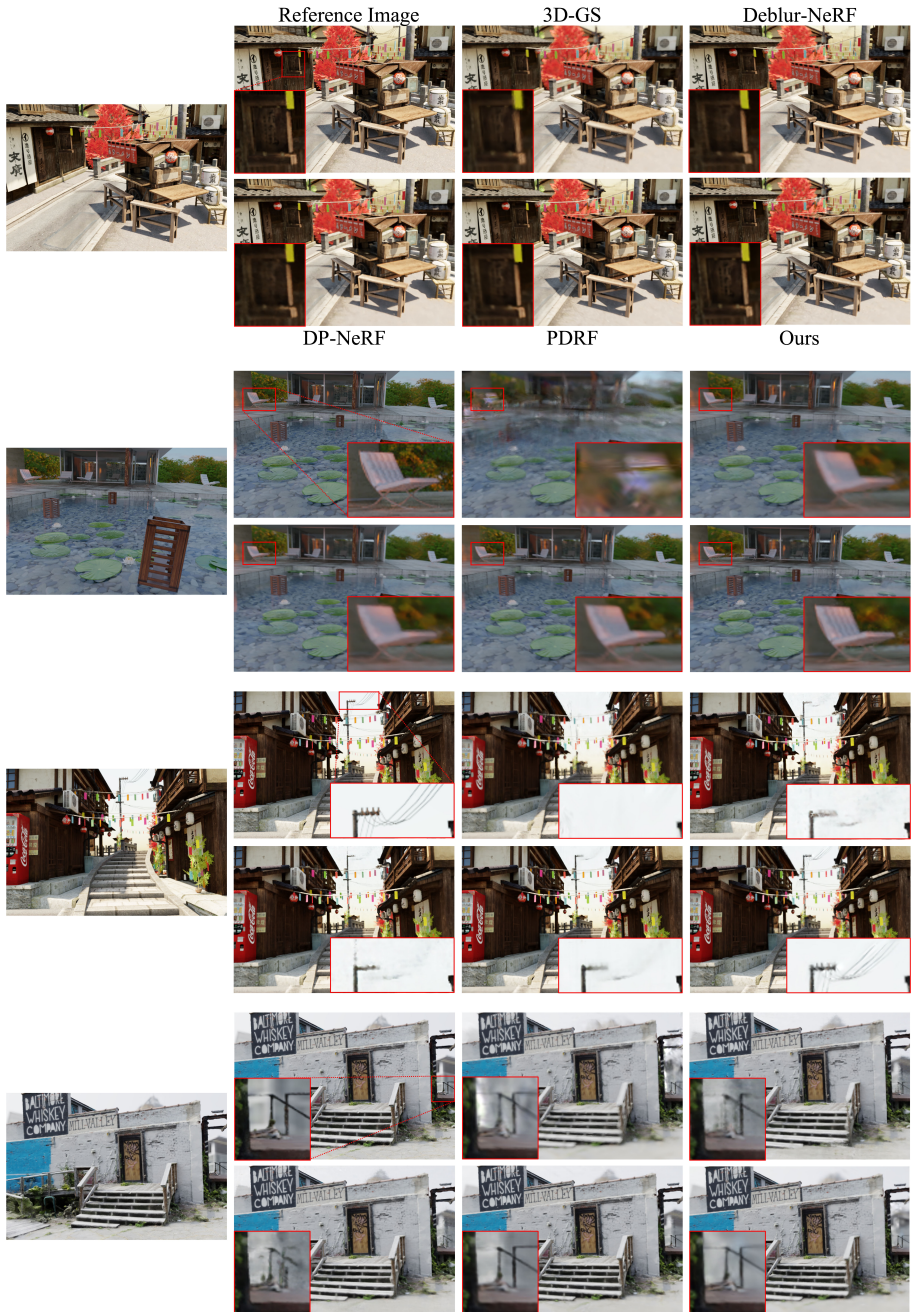


Table 3. Transformation of two attributes (scale and rotation) of 3D Gaussians to model the blur.

	train	test
scale	0.87	0.85
rotation	0.26	0.25

Table 4. Ablation study on adding the extra points. w/ Random Colors stands for uniformly allocating points to the point cloud but color features are randomly initialized, rather than interpolated from neighboring points.

Methods	PSNR \uparrow	SSIM \uparrow
w/o Extra Points	22.56	0.7016
w/ Random Colors	22.90	0.7089
w/ Extra Points	23.80	0.7430

Table 5. Ablation study on depth-depending pruning. Naive pruning stands for using naive points pruning from 3D-GS and Depth-based pruning stands for applying our depth-based pruning.

Methods	PSNR \uparrow	SSIM \uparrow
Naive pruning	23.33	0.7296
Depth-based pruning	23.80	0.7430

5 Limitations & Future Works

NeRF-based deblurring methods [22,20,28], which are developed under the assumption of volumetric rendering, are not straightforwardly applicable to rasterization-based 3D-GS [15]. However, they can be compatible to rasterization by optimizing their MLP to deform kernels in the space of the rasterized image instead of letting MLP deform the rays and kernels in the world space. Although it is an interesting direction, it will incur additional costs for interpolating pixels and just implicitly transform the geometry of 3D Gaussians. Therefore, we believe that it will not be an optimal way to model scene blurriness using 3D-GS [15]. Another approach to deblur the defocus blur using 3D-GS [15] can be convolving the rasterized image with conventional grid blur kernels such as gaussian blur kernel [14]. With this approach however, the kernel expressivity is limited compared to the learnable kernels since the Gaussian blur kernel is a simple unimodal Gaussian distribution along each axis and is not learnable. Instead of a fixed Gaussian blur kernel, adopting a learnable grid blur kernel can also be another promising direction to address defocus blur. Nevertheless, as blurriness naturally varies spatially across the scene and each pixel, it is ideal to train blur kernels for every pixel from all training views. Thus, such method can incur high memory requirements, and its usage is limited if the rendering image is high resolution or lots of training images are provided.

6 Conclusion

We proposed Deblurring 3D-GS, the first defocus deblurring algorithm for 3D-GS. We adopted a small MLP that transforms the 3D Gaussians to model the scene blurriness. We also further facilitate deblurring by densifying sparse point clouds from blurry input images through additional point allocation, which uniformly distributes points in the scene and assigns color features using the K-Nearest-Neighbor algorithm. Also, as we applied depth-based pruning instead of naive pruning, which 3D-GS has adopted, we could preserve more points at the far edge of the scene where SfM usually struggles to extract features and fails to generate enough points. Through extensive experiments, we validated that our method can deblur the defocus blur while still enjoying the real-time rendering with FPS > 200. This is because we use the MLP only during the training time, and the MLP is not involved in the inference stage, keeping the inference stage identical to the 3D-GS. Our method achieved state-of-the-art performance or performed comparably with current cutting-edge models evaluated under different metrics.

References

1. Abuolaim, A., Afifi, M., Brown, M.S.: Improving single-image defocus deblurring: How dual-pixel images help through multi-task learning. In: Proceedings of the IEEE/CVF Winter Conference on Applications of Computer Vision. pp. 1231–1239 (2022) [4](#)
2. Barron, J.T., Mildenhall, B., Verbin, D., Srinivasan, P.P., Hedman, P.: Zip-nerf: Anti-aliased grid-based neural radiance fields. ICCV (2023) [5](#)
3. Cao, A., Johnson, J.: Hexplane: A fast representation for dynamic scenes. CVPR (2023) [5](#)
4. Chen, A., Xu, Z., Geiger, A., Yu, J., Su, H.: Tensorf: Tensorial radiance fields. In: Computer Vision—ECCV 2022: 17th European Conference, Tel Aviv, Israel, October 23–27, 2022, Proceedings, Part XXXII. pp. 333–350. Springer (2022) [5](#)
5. Community, B.O.: Blender - a 3D modelling and rendering package. Blender Foundation, Stichting Blender Foundation, Amsterdam (2018), <http://www.blender.org> [12](#)
6. Dai, P., Zhang, Y., Yu, X., Lyu, X., Qi, X.: Hybrid neural rendering for large-scale scenes with motion blur. In: Proceedings of the IEEE/CVF Conference on Computer Vision and Pattern Recognition (2023) [2, 6](#)
7. Drebin, R.A., Carpenter, L., Hanrahan, P.: Volume rendering. ACM Siggraph Computer Graphics **22**(4), 65–74 (1988) [2, 5](#)
8. Fridovich-Keil, S., Meanti, G., Warburg, F.R., Recht, B., Kanazawa, A.: K-planes: Explicit radiance fields in space, time, and appearance. In: CVPR (2023) [2, 5](#)
9. Fridovich-Keil, S., Yu, A., Tancik, M., Chen, Q., Recht, B., Kanazawa, A.: Plenoxels: Radiance fields without neural networks. In: Proceedings of the IEEE/CVF Conference on Computer Vision and Pattern Recognition. pp. 5501–5510 (2022) [2](#)
10. Garbin, S.J., Kowalski, M., Johnson, M., Shotton, J., Valentin, J.: Fastnerf: High-fidelity neural rendering at 200fps. In: Proceedings of the IEEE/CVF International Conference on Computer Vision. pp. 14346–14355 (2021) [2](#)
11. Glorot, X., Bengio, Y.: Understanding the difficulty of training deep feedforward neural networks. In: Proceedings of the thirteenth international conference on artificial intelligence and statistics. pp. 249–256. JMLR Workshop and Conference Proceedings (2010) [11](#)
12. Hecht, E.: Optics. Pearson Education India (2012) [7](#)
13. Hedman, P., Srinivasan, P.P., Mildenhall, B., Barron, J.T., Debevec, P.: Baking neural radiance fields for real-time view synthesis. ICCV (2021) [5](#)

14. Hummel, R.A., Kimia, B., Zucker, S.W.: Deblurring gaussian blur. *Computer Vision, Graphics, and Image Processing* **38**(1), 66–80 (1987) [16](#)
15. Kerbl, B., Kopanas, G., Leimkühler, T., Drettakis, G.: 3d gaussian splatting for real-time radiance field rendering. *ACM Transactions on Graphics (ToG)* **42**(4), 1–14 (2023) [2](#), [3](#), [5](#), [6](#), [7](#), [9](#), [10](#), [11](#), [16](#)
16. Kingma, D., Ba, J.: Adam: A method for stochastic optimization. In: *International Conference on Learning Representations (ICLR)* (2015) [11](#)
17. Kuipers, J.B.: *Quaternions and rotation sequences: a primer with applications to orbits, aerospace, and virtual reality*. Princeton university press (1999) [6](#)
18. Kundur, D., Hatzinakos, D.: Blind image deconvolution. *IEEE signal processing magazine* **13**(3), 43–64 (1996) [4](#)
19. Lee, D., Lee, M., Shin, C., Lee, S.: Deblurred neural radiance field with physical scene priors. *arXiv preprint arXiv:2211.12046* (2022) [5](#), [11](#)
20. Lee, D., Lee, M., Shin, C., Lee, S.: Dp-nerf: Deblurred neural radiance field with physical scene priors. In: *Proceedings of the IEEE/CVF Conference on Computer Vision and Pattern Recognition (CVPR)*. pp. 12386–12396 (June 2023) [2](#), [11](#), [16](#)
21. Liu, Y.Q., Du, X., Shen, H.L., Chen, S.J.: Estimating generalized gaussian blur kernels for out-of-focus image deblurring. *IEEE Transactions on circuits and systems for video technology* **31**(3), 829–843 (2020) [4](#)
22. Ma, L., Li, X., Liao, J., Zhang, Q., Wang, X., Wang, J., Sander, P.V.: Deblur-nerf: Neural radiance fields from blurry images. In: *Proceedings of the IEEE/CVF Conference on Computer Vision and Pattern Recognition*. pp. 12861–12870 (2022) [2](#), [5](#), [10](#), [11](#), [12](#), [16](#)
23. Mildenhall, B., Srinivasan, P.P., Tancik, M., Barron, J.T., Ramamoorthi, R., Ng, R.: Nerf: Representing scenes as neural radiance fields for view synthesis. In: *ECCV* (2020) [1](#), [2](#), [5](#), [8](#), [11](#)
24. Müller, T., Evans, A., Schied, C., Keller, A.: Instant neural graphics primitives with a multiresolution hash encoding. *ACM Transactions on Graphics (ToG)* **41**(4), 1–15 (2022) [2](#), [5](#)
25. Nimisha, T.M., Kumar Singh, A., Rajagopalan, A.N.: Blur-invariant deep learning for blind-deblurring. In: *Proceedings of the IEEE international conference on computer vision*. pp. 4752–4760 (2017) [5](#)
26. Pan, J., Sun, D., Pfister, H., Yang, M.H.: Blind image deblurring using dark channel prior. In: *Proceedings of the IEEE conference on computer vision and pattern recognition*. pp. 1628–1636 (2016) [4](#)
27. Paszke, A., Gross, S., Massa, F., Lerer, A., Bradbury, J., Chanan, G., Killeen, T., Lin, Z., Gimelshein, N., Antiga, L., et al.: Pytorch: An imperative style, high-performance deep learning library. *Advances in Neural Information Processing Systems* **32** (2019) [11](#)
28. Peng, C., Chellappa, R.: Pdrf: Progressively deblurring radiance field for fast and robust scene reconstruction from blurry images (2022) [2](#), [5](#), [11](#), [16](#)
29. Peterson, L.E.: K-nearest neighbor. *Scholarpedia* **4**(2), 1883 (2009) [4](#), [10](#)
30. Reiser, C., Szeliski, R., Verbin, D., Srinivasan, P.P., Mildenhall, B., Geiger, A., Barron, J.T., Hedman, P.: Merf: Memory-efficient radiance fields for real-time view synthesis in unbounded scenes. *SIGGRAPH* (2023) [5](#)
31. Ren, D., Zhang, K., Wang, Q., Hu, Q., Zuo, W.: Neural blind deconvolution using deep priors. In: *Proceedings of the IEEE/CVF Conference on Computer Vision and Pattern Recognition*. pp. 3341–3350 (2020) [5](#)
32. Rho, D., Lee, B., Nam, S., Lee, J.C., Ko, J.H., Park, E.: Masked wavelet representation for compact neural radiance fields. In: *Proceedings of the IEEE/CVF Conference on Computer Vision and Pattern Recognition (CVPR)*. pp. 20680–20690 (June 2023) [5](#)
33. Richardson, W.H.: Bayesian-based iterative method of image restoration. *JoSA* **62**(1), 55–59 (1972) [4](#)

34. Ruan, L., Chen, B., Li, J., Lam, M.: Learning to deblur using light field generated and real defocus images. In: Proceedings of the IEEE/CVF Conference on Computer Vision and Pattern Recognition. pp. 16304–16313 (2022) [4](#)
35. Schonberger, J.L., Frahm, J.M.: Structure-from-motion revisited. In: Proceedings of the IEEE conference on computer vision and pattern recognition. pp. 4104–4113 (2016) [3](#), [6](#)
36. Schönberger, J.L., Frahm, J.M.: Structure-from-motion revisited. In: Conference on Computer Vision and Pattern Recognition (CVPR) (2016) [10](#), [12](#)
37. Schönberger, J.L., Zheng, E., Pollefeys, M., Frahm, J.M.: Pixelwise view selection for unstructured multi-view stereo. In: European Conference on Computer Vision (ECCV) (2016) [12](#)
38. Sun, C., Sun, M., Chen, H.T.: Direct voxel grid optimization: Super-fast convergence for radiance fields reconstruction. In: Proceedings of the IEEE/CVF Conference on Computer Vision and Pattern Recognition. pp. 5459–5469 (2022) [2](#), [5](#)
39. Tancik, M., Srinivasan, P., Mildenhall, B., Fridovich-Keil, S., Raghavan, N., Singhal, U., Ramamoorthi, R., Barron, J., Ng, R.: Fourier features let networks learn high frequency functions in low dimensional domains. *Advances in Neural Information Processing Systems* **33**, 7537–7547 (2020) [5](#)
40. Wang, P., Liu, Y., Chen, Z., Liu, L., Liu, Z., Komura, T., Theobalt, C., Wang, W.: F2-nerf: Fast neural radiance field training with free camera trajectories. *CVPR* (2023) [5](#)
41. Wang, P., Zhao, L., Ma, R., Liu, P.: Bad-nerf: Bundle adjusted deblur neural radiance fields. *arXiv preprint arXiv:2211.12853* (2022) [2](#), [6](#)
42. Whyte, O., Sivic, J., Zisserman, A., Ponce, J.: Non-uniform deblurring for shaken images. *International journal of computer vision* **98**, 168–186 (2012) [4](#)
43. Wu, Z., Li, X., Peng, J., Lu, H., Cao, Z., Zhong, W.: Dof-nerf: Depth-of-field meets neural radiance fields. In: Proceedings of the 30th ACM International Conference on Multimedia. pp. 1718–1729 (2022) [2](#), [5](#)
44. Xu, L., Zheng, S., Jia, J.: Unnatural l0 sparse representation for natural image deblurring. In: Proceedings of the IEEE conference on computer vision and pattern recognition. pp. 1107–1114 (2013) [4](#)
45. Yariv, L., Hedman, P., Reiser, C., Verbin, D., Srinivasan, P.P., Szeliski, R., Barron, J.T., Mildenhall, B.: Bakedsd: Meshing neural sdfs for real-time view synthesis. *arXiv* (2023) [5](#)
46. Zhang, H., Dai, Y., Li, H., Koniusz, P.: Deep stacked hierarchical multi-patch network for image deblurring. In: Proceedings of the IEEE/CVF Conference on Computer Vision and Pattern Recognition. pp. 5978–5986 (2019) [5](#)
47. Zhang, M., Fang, Y., Ni, G., Zeng, T.: Pixel screening based intermediate correction for blind deblurring. In: Proceedings of the IEEE/CVF Conference on Computer Vision and Pattern Recognition. pp. 5892–5900 (2022) [4](#)
48. Zwicker, M., Pfister, H., Van Baar, J., Gross, M.: Ewa splatting. *IEEE Transactions on Visualization and Computer Graphics* **8**(3), 223–238 (2002) [6](#)